Materials Horizons

ROYAL SOCIETY OF CHEMISTRY

COMMUNICATION

View Article Online
View Journal | View Issue

Cite this: *Mater. Horiz.*, 2022, 9, 342

Received 25th March 2021,
Accepted 1st July 2021

DOI: 10.1039/d1mh00508a

rsc.li/materials-horizons

3D printing of artificial skin patches with bioactive and optically active polymer materials for anti-infection and augmenting wound repair†

Hao Zhao, ‡[ad] Jingwen Xu,‡[bc] Haitao Yuan,[a] Endong Zhang,[ad] Nan Dai,[ad] Zhiqiang Gao,[ad] Yiming Huang,[a] Fengting Lv,[a] Libing Liu,[ad] Qi Gu *[bc] and Shu Wang *[ad]

A printable ink composed of a photoactive cationic conjugated poly(phenylene vinylene) derivative (PPV) and gelatin/alginate/hyaluronic acid is developed for 3D printing artificial skin patches. This patch shows excellent photodynamic therapy-based anti-infection superiority and outstanding bioactivity to facilitate wound repair. This study contributes to design new conjugated polymer inks for manufacturing functional skin patches.

New concepts

Inspired by the skin biofunction of protecting the body from microorganism invasion, artificially manufacturing human skin *in vitro* with promising anti-infection capability and skin regeneration ability is urgently required in wound repair. Here, a printable ink composed of natural biomacromolecules, namely gelatin (Gel), alginate (Alg), hyaluronic acid (HA) and a photoactive cationic conjugated poly(phenylene vinylene) derivative (PPV), was developed for the 3D printing of artificial skin patches. Compared to the FDA-proved anionic photosensitizer verteporfin, cationic PPV exhibits lower cytotoxicity, promising visible light-harvest ability and strong electrostatic interactions with the printing matrix, endowing the artificial skin patches with excellent photodynamic therapy (PDT)-based anti-infection superiority against *Staphylococcus aureus in vitro* and *in vivo*. Besides, laminin-derived peptide A5G81 was further covalently modified to the artificial skin patches, which displayed outstanding biocompatibility, cell migration and attachment-promoted effects, thereby facilitating to wound healing *in vivo*. Compared to other hydrogel system-based dressings, the developed skin patches herein with integrated antibacterial ability, tissue regeneration-promoted capacity and plenty of microstructure styles were more suitable to work as skin equivalents when a skin trauma occurred. This study provides an advanced conjugated polymer ink for skin repair by 3D printing.

Patients undergoing skin damages, including violent mechanical trauma, unavoidable surgical procedures and extensive burns, may be left with life-threatening risks due to the emergent haemorrhagic shock, severe fluid loss and multiple microorganism infections.[1–3] As human body's primary defence against the adverse environment, once the skin trauma occurs, the soft tissue regeneration always features with time-consumption and complexity.[4] Under this condition, a skin substitute is anticipated to be fabricated for protecting the human body from external stimulations, facilitating wound healing. Assisted by the extracellular matrix (ECM)-like properties, recently emerging hydrogel systems provide new opportunities for tissue engineering, particularly to manufacture skin substitutes for combating microorganism infection and shortening the regeneration process.[5–9] However, most reported hydrogels do not possess flexible and precise microstructures, which limit their oxygen permeability and structure diversity. Thus, constructing an artificial skin patch with flexible and precise microstructures as well as anti-infection and regeneration-promoted functions is urgently desirable.

3D printing has grown to be one of the most potential biomanufacturing technologies owing to its advanced precision, smart flexibility and tailored functionality,[10,11] which was successfully demonstrated by inspiring *in vitro* fabrications of heart,[12] lung,[13] ovary[14] and spinal cord.[15] Impressive achievements in skin reconstruction have also been realized including a skin tissue regeneration method by laser cell printing,[16] a scaffold-free approach for human skin 3D printing[17] and a robust platform for engineering human skin equivalents.[18] Notably, the highly porous and ordered artificial skin patches fabricated by 3D printing can divide the large skin trauma into pieces of tiny wounds to guide the healing process, and also provide a migration scaffold for multiple skin cells to accelerate the wound repair.[19–21] Therefore, 3D

[a] *Beijing National Laboratory for Molecular Sciences, Key Laboratory of Organic Solids, Institute of Chemistry, Chinese Academy of Sciences, Beijing 100190, P. R. China. E-mail: wangshu@iccas.ac.cn*
[b] *State Key Laboratory of Membrane Biology, Institute of Zoology, Chinese Academy of Sciences, Beijing 100101, P. R. China. E-mail: qgu@ioz.ac.cn*
[c] *Institute for Stem Cell and Regeneration, Chinese Academy of Sciences, Beijing 100101, China*
[d] *College of Chemistry, University of Chinese Academy of Sciences, Beijing 100049, P. R. China*

† Electronic supplementary information (ESI) available. See DOI: 10.1039/d1mh00508a

‡ H. Z. and J. X. contributed equally to this work.

printing can be considered as a feasible strategy to manufacture a biomimetic human skin patch offering the dual functions of anti-infection and promoting regeneration.

Natural biomacromolecule gelatin mixed with alginate (Gel/Alg) has proven to be an ideal ink candidate owing to its favorable biocompatibility together with biodegradability *in vitro* and *in vivo*, where Gel provides the promising 3D printability, while Alg is for crosslinking.[22,23] Moreover, hyaluronic acid (HA), as a vital component of ECM, can also improve wound repair by augmenting cell migration in addition to inducing morphogenesis and matrix reorganization.[8,24] Gel/Alg along with HA (Gel/Alg/HA) may contribute to the human skin reconstruction by 3D printing. For overcoming the severe infection in the damaged skin, diverse antibacterial hydrogels are constantly proposed.[25,26] However, antibiotic-immobilized hydrogels should be seriously utilized due to the problems of multidrug resistance and relatively long treatment course, while hydrogels loaded with noble metal nanoparticles often cause undesirable systemic toxicity. Recently, inherent antibacterial materials including quaternary ammonium polymers,[3] polyphenol-amyloid fibril hydrogels[27] and antibacterial peptides,[28] have exhibited good cell safety as well as promising antibacterial efficiency. In addition, photodynamic therapy (PDT) has stood out from the emerging antibacterial therapeutics due to its high antibacterial efficiency, short treatment period, minimal side effects and negligible drug resistance.[29] Conjugated polymers, with an extended π-conjugation degree and strong light-harvest/photosensitization capabilities, have been regarded as robust therapeutic tools for antibacterial and anticancer treatments.[30,31] They can sensitize the surrounding oxygen to generate cytotoxic reactive oxygen species (ROS), subsequently leading to photo-triggered cell death.[32] With improved water-solubility, cationic conjugated polymers deserve to be integrated into Gel/Alg/HA-based ink for fabricating antibacterial skin patches, aiming to impart the patches with promising PDT effects. Besides, the electrostatic interaction between cationic conjugated polymers and anionic Gel/Alg/HA can facilitate the formation of uniform ink systems for developing new functional conjugated polymer inks. Moreover, high cell affinity inks to fabricate artificial skin patches are also anticipated for significantly improving the healing rate. Recently, a laminin-derived peptide, namely A5G81 (AGQWHRVSVRWGC), has been reported to work as a cell adhesion domain that specifically binds to integrins $\alpha_3\beta_1$ and $\alpha_6\beta_1$, which is different from the widely used RGD peptides. The covalent modification of A5G81 to 3D printing inks would augment skin regeneration by enhancing cell adhesion, migration, and proliferation.[33]

In this study, we incorporated a photoactive cationic conjugated poly(phenylene vinylene) derivative (PPV, chemical structure is shown in Scheme 1 and Fig. 1a) into the 3D printing ink Gel/Alg/HA to develop a newly conjugated polymer ink Gel/Alg/HA/PPV, which was utilized to fabricate artificial skin patches for wound repair by 3D printing (Scheme 1). Cationic PPV exhibits stronger visible light-harvest and higher ROS generation abilities together with excellent biocompatibility than the FDA-approved anionic photosensitizer verteporfin (Ver). The electrostatic

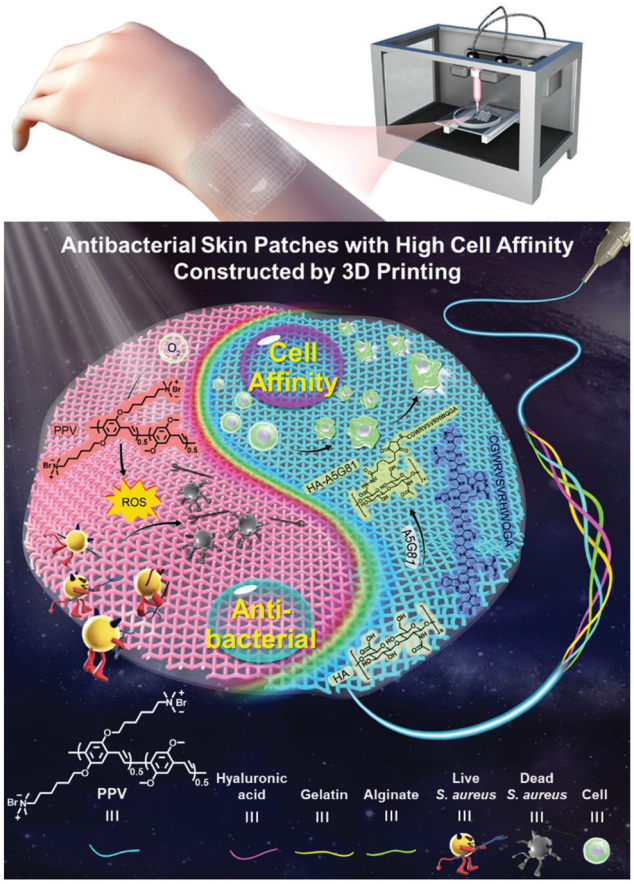

Scheme 1 Schematic of the 3D printed antibacterial skin patches with high cell affinity for augmenting wound repair based on the conjugated polymer ink.

interaction between cationic PPV and anionic Gel/Alg/HA could assist the formation of a uniform ink system and reduce its toxicity. Antibacterial skin patches printed from Gel/Alg/HA/PPV displayed outstanding PDT-based anti-infection superiorities against *Staphylococcus aureus* (*S. aureus*) *in vitro* and *in vivo*. Moreover, the incorporation of a laminin-derived peptide, A5G81, to the skin patches indeed accelerated the wound healing *in vivo* by augmenting cell adhesion and migration. This study reports a new functional conjugated polymer ink for 3D printing in tissue engineering, particularly in manufacturing artificial skin patches for anti-infection and augmenting wound repair.

Conjugated polymer PPV was selected as a photo-active material to fabricate antibacterial skin patch, while an FDA-approved second generation of porphyrin photosensitizer Ver was chosen for comparison. The chemical structures of PPV and Ver are illustrated in Fig. 1a and b, respectively. As shown in Fig. 1c, the absorption of PPV mainly located in the visible light region, indicating that PPV could be excited by sunlight for ROS generation, while Ver possessed the light-harvesting ability both in the visible and near-infrared regions. PPV existed in water as aggregates with a size of 76.6 ± 1.1 nm and displayed a zeta potential of +38.7 ± 1.0 mV because of the presence of cationic side chains. Ver was negatively charged with a zeta potential of −32.0 ± 0.6 mV and exhibited larger

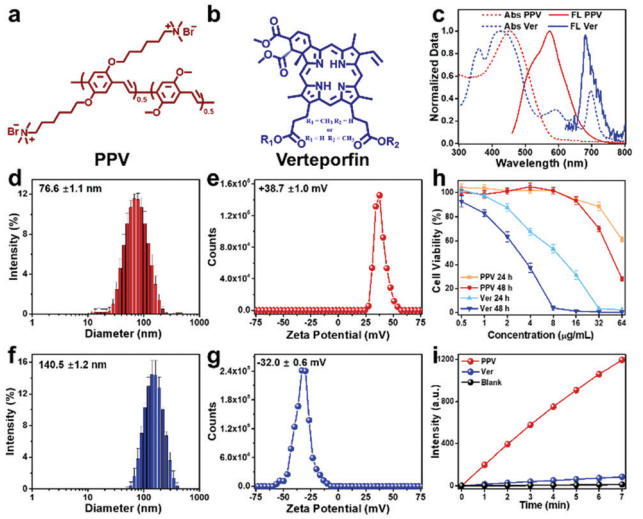

Fig. 1 Property comparisons of PPV and Ver. Chemical structure of (a) PPV and (b) Ver. (c) Normalized absorption and emission spectra of PPV and Ver. (d) Dynamic light scattering and (e) zeta potential data of PPV in water, [PPV] = 1 μg mL^{-1}. (f) Dynamic light scattering and (g) zeta potential data of Ver in water, [Ver] = 1 μg mL^{-1}. (h) Cell viability after the treatment with various concentrations of PPV and Ver for 24 h and 48 h, respectively. (i) Fluorescence intensity of the DCFH solution after the addition of PPV and Ver, respectively, under white light irradiation (10 mW cm^{-2}) with an excitation of 488 nm. [PPV] = [Ver] = 1 μg mL^{-1}.

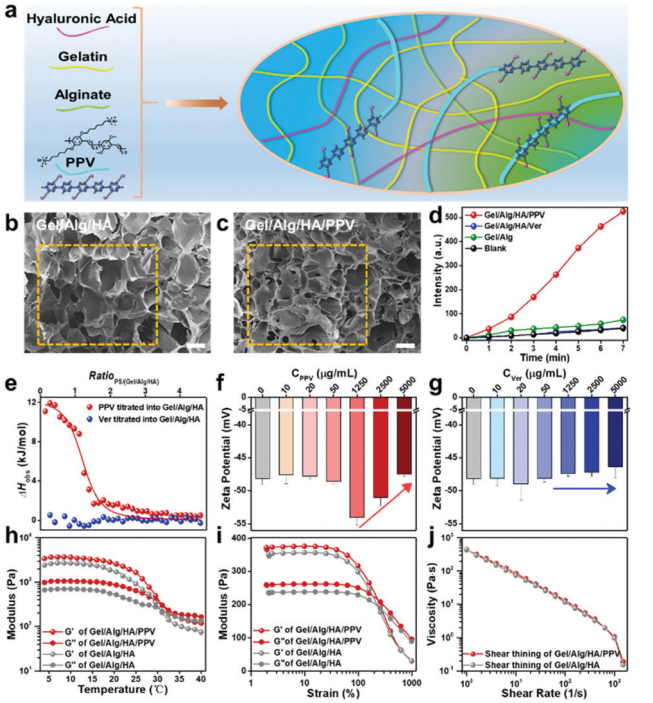

Fig. 2 Preparation of the Gel/Alg/HA/PPV ink and the studies of the interaction mechanisms. (a) Preparation scheme of the Gel/Alg/HA/PPV ink. FSEM images of the Ca^{2+}-crosslinked (b) Gel/Alg/HA (4% w/v Gel + 2% w/v Alg + 1% w/v HA) and (c) Gel/Alg/HA/PPV (4% w/v Gel + 2% w/v Alg + 1% w/v HA + 300 μg mL^{-1}) ink, scale bar: 200 μm. (d) Fluorescence intensity of the DCFH solution after the addition of PPV and Ver skin patches, respectively, under white light irradiation (10 mW cm^{-2}) with an excitation of 488 nm. (e) ITC fitting data for the titration of the PPV solution (5 mM) or Ver solution (5 mM) into the Gel/Alg/HA solution (mass ratio of Gel to Alg and HA is 4 : 2 : 1, 0.6 mM Alg in repeat units). Zeta potentials of the Gel/Alg/HA ink treated with various concentrations of (f) PPV and (g) Ver, respectively. Rheological characterization as a function of (h) temperature and (i) strain, and (j) shear thinning property of the Gel/Alg/HA and Gel/Alg/HA/PPV ink, respectively.

aggregates with a size of 140.5 ± 1.2 nm (Fig. 1f and g). Owing to the anionic characteristic of the Gel/Alg/HA ink, cationic polymer PPV could be electrostatically combined with Gel/Alg/HA to form a uniformly conjugated polymer ink system without distinct diffusion, which was the first advantage of PPV over the anionic small molecule Ver. Biocompatibility, particularly the cell safety, is an important point to be considered in selecting a suitable photosensitizer. As shown in Fig. 1h, Ver could cause more severe cytotoxicity towards human umbilical cord-derived mesenchymal stem cells (hMSCs). However, PPV exhibited a high cell safety, even at high concentrations, which was the second advantage of PPV over Ver. Subsequently, 2,7-dichlorodihydrofluorescein (DCFH) assay was performed to characterize the ROS-production ability of PPV and Ver, respectively. According to the data presented in Fig. 1i, under the same conditions, PPV could generate more ROS over Ver, which was the third advantage.

To develop a new printable ink for antibacterial skin patch fabrication by 3D printing, cationic PPV was mixed with anionic Gel/Alg/HA to prepare a Gel/Alg/HA/PPV ink, and the preparation scheme is illustrated in Fig. 2a. Ver was introduced to Gel/Alg/HA in the same manner. As shown in Fig. 2b, field emission scanning electron microscopy (FSEM) images of Gel/Alg/HA show that the ink displayed a highly porous microstructure with an average pore size of ~200 μm. The incorporation of PPV made the porous microstructure a little denser (Fig. 2c). Being well consistent with the results in Fig. 1i, the ROS-production ability of the Gel/Alg/HA/PPV skin patch was still better than that of Gel/Alg/HA/Ver after 3D printing (Fig. 2d). To investigate the electrostatic interaction between cationic PPV and anionic Gel/Alg/HA, isothermal titration calorimetry (ITC) and zeta potential studies were performed accordingly. As shown in Fig. 2e, upon titrating PPV into Gel/Alg/HA, the observed enthalpy change (ΔH_{obs}) was positive, indicating an endothermic process. The binding affinity of PPV towards Gel/Alg/HA was calculated to be 3.3×10^4 M^{-1}. In general, the electrostatic interaction exhibits an exothermic process, but the heat released by the Gel/Alg/HA/PPV complex was covered by the heat absorbed when counterions and bound water were released, thereby showing a positive ΔH_{obs}. Due to the negative charge on Ver, there was no obvious enthalpy change in the titration process, suggesting an inapparent interaction between Ver and Gel/Alg/HA. The robust electrostatic interaction could help bioactive PPV to tightly combine with Gel/Alg/HA to form a uniformly conjugated polymer ink without distinct diffusion of PPV, so that reduced its systemic toxicity. Fig. 2f displays the zeta potential value changes of Gel/Alg/HA after the addition of various concentrations of PPV. Adding a low concentration of PPV caused insignificant zeta potential value changes. When adding more PPV with a final concentration of 1250 μg mL^{-1}, the zeta potential displayed a negative movement

from −48.6 ± 0.4 mV to −54.0 ± 1.2 mV due to the higher negative charge density of anionic Gel/Alg/HA on the outer surface of the PPV aggregates. A positive movement of the zeta potential value was subsequently observed after continuously increasing the PPV concentration, suggesting electrostatic interaction between cationic PPV and anionic Gel/Alg/HA. As shown in Fig. 2g, the negligible zeta potential changes in the Ver titration process demonstrate an insufficient interaction between Ver and the ink matrix, which was well consistent with the results presented in Fig. 2e. It should be noted that assisted by the tight electrostatic interaction between PPV and Gel/Alg/HA, the dynamic modulus as the function of temperature (Fig. 2h) and strain (Fig. 2i) was improved, while the phase transition points and shear thinning property (Fig. 2j) were not dramatically influenced after incorporating with PPV. Diffusion studies of PPV from the Gel/Alg/HA/PPV ink were subsequently investigated. The PPV diffusion from the Gel/Alg/HA/PPV ink was monitored by measuring its fluorescence intensity in the printed structure-immersed solutions. As shown in Fig. S1 (ESI†), no apparent diffusion of PPV was observed even after 24 h of soaking because of the low florescence intensity. The negligible PPV diffusion reached equilibrium after 2 h. Besides, the color of the printed structures before and after the 24 h soaking remained unchanged. It was because the strong electrostatic interaction assisted the cationic PPV to tightly combine with the ionic Gel/Alg/HA matrix, which indeed avoided the rapid diffusion and also presented a feasible strategy for ink functionalization.

To investigate the 3D printability of the proposed Gel/Alg/HA/PPV ink and the tailored microstructure of artificial skin patches, a series of printing tests were conducted. The printing process with a commercial 3D printer is shown in Fig. 3a. Fig. 3b shows the printed large-size artificial skin patch from the Gel/Alg/HA/PPV ink, which could be stretched to a certain extent, indicating its flexibility. The letter patterns of "ICCAS" with self-support and well-defined boundary capabilities were printed from the Gel/Alg/HA/PPV ink, further indicating its excellent 3D printability. With the help of its inherent fluorescence of PPV, the "ICCAS" pattern could be visible under excitation, implying the potential of the imaging ability (Fig. 3c and d). More importantly, to diversify their microstructures, artificial skin patches with 30°, 60° and 90° pore geometries were fabricated by manipulating the angles between the neighboring layers. The pattern diagram, digital and fluorescence images of these printed skin patches are displayed in Fig. 3e–g, respectively. Subsequently, the tensile tests of the printed Gel/Alg/HA/PPV patches with 30°, 60° and 90° pore geometries were performed after 3D printing to characterize their mechanical properties. As shown in Fig. S2 (ESI†), the tensile modulus decreased in the sequence of 60°, 30° and 90°, indicating that the skin patches with the 90° pore geometry were the most stretchable. The result was well consistent with the data presented in Fig. 3b. Thus, the patch microstructures could be successfully customized by the 3D printing strategy relying on its outstanding spatiotemporal controllability. The adjustable microstructures definitely enriched the skin patch styles.

Motivated by the promising ROS-generation capability and excellent printability of the Gel/Alg/HA/PPV ink along with the diverse microstructures of the developed PPV skin patches, their photodynamic antibacterial performance was investigated. Considering its clinical significance, Gram-positive *S. aureus* was selected for the *in vitro* anti-infection experiments. As shown in Fig. 4a and b, in the absence of PPV skin patches, *S. aureus* grew and proliferated smoothly both in dark and under white light irradiation. The dark toxicity of the PPV skin patches towards *S. aureus* was also inconspicuous. When increasing the concentrations of PPV in skin patches to 100 μg mL^{-1}, 200 μg mL^{-1} and 300 μg mL^{-1}, the bacterial killing efficiencies of PPV skin patches towards *S. aureus* under light irradiation (60 mW cm^{-2}) were 6.8%, 72.9% and 89.4% respectively, indicating an excellent and concentration-dependent antibacterial efficacy *in vitro*. Subsequently, *S. aureus*-infected rat wound models were utilized in order to further evaluate the antibacterial efficiency of the PPV skin patches *in vivo*. Fig. 4c illustrates the process of investigating the antibacterial effects of PPV skin patches against *S. aureus in vivo*. The images of the infected wounds at different observation time points are shown in Fig. 4d. All the wounds before

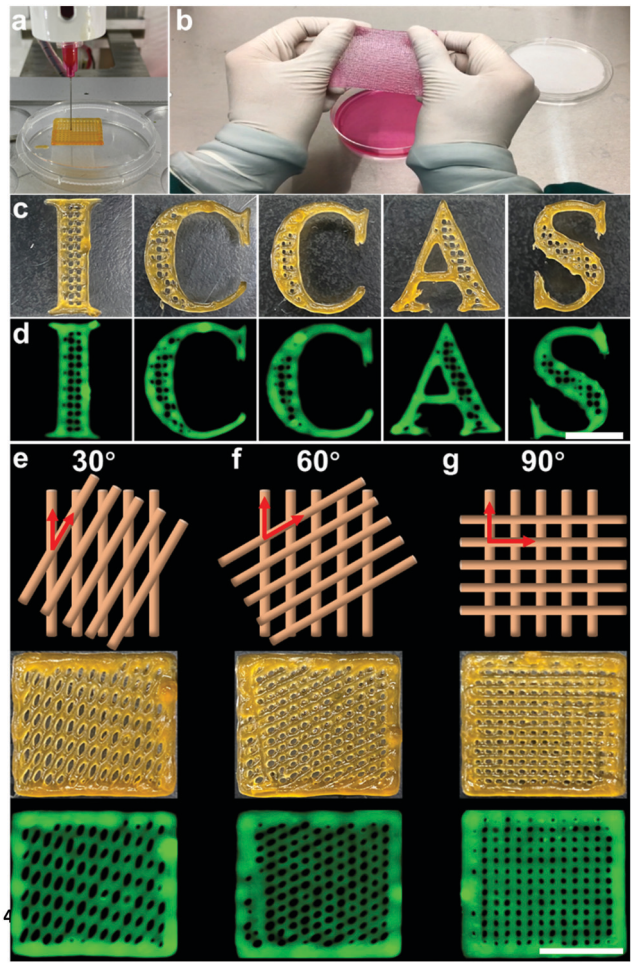

Fig. 3 3D architectures printed from the Gel/Alg/HA/PPV ink. (a) Digital images showing the 3D printing process. (b) The 3D printed large size antibacterial skin patch. (c) Digital and (d) fluorescence images of "ICCAS" letters printed from the Gel/Alg/HA/PPV ink, scale bar: 1 cm. Pattern diagram, digital and fluorescence images of 3D printed structures with (e) 30°, (f) 60° and (g) 90° pore geometry, scale bar: 1 cm.

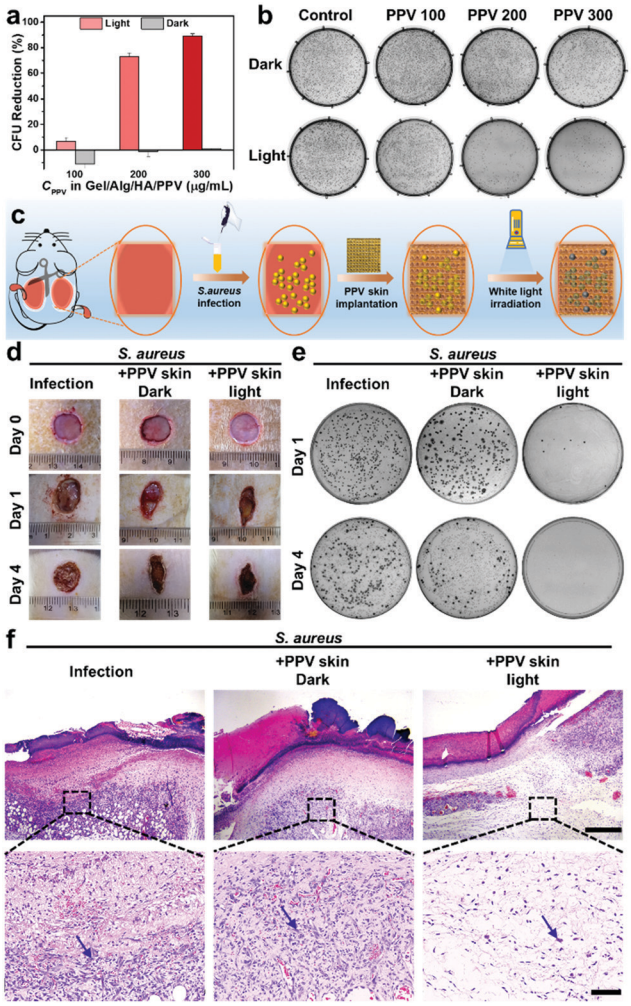

Fig. 4 Antibacterial efficiency of Gel/Alg/HA/PPV skin patches *in vitro* and *in vivo*. (a) Reduction of colony forming units (CFU) of *S. aureus* under various treatments *in vitro*. (b) Photographs of CFU on the agar plates of *S. aureus* under various treatments *in vitro*. The concentrations of PPV in PPV skin patches were set as 100, 200 and 300 μg mL^{-1}, respectively. (c) Schematic of investigating the antibacterial effects of PPV skin patches by a *S. aureus*-infected wound model on rats. (d) Photographs of *S. aureus*-infected wounds after various treatments with Gel/Alg/HA/PPV skin patches under white irradiation (60 mW cm^{-2}) for 30 min on day 1 and day 4 post-infection. (e) Photographs of CFU on the agar plates of *S. aureus* originating from the infected sites on rats under various treatments. (f) H&E staining of the infected wound tissues on rats after day 4 post-infection, the inflammatory cells were stained blue and indicated with arrows, scale bar: 500 μm and 100 μm, respectively.

infections were clean and healthy. On day 1 post-infection, the infection group without any treatment displayed the sign of suppuration, and the situation got more serious on day 4 post-infection. The *S. aureus*-infected wounds on the PPV skin patch dark group show a wet wound site and also displayed a slight sign of suppuration on day 1 post-infection, while the wounds were wet and got suppuration on the edge of the wounds on day 4 post-infection. Inspiringly, upon photodynamic therapeutics of the PPV skin patches after infected with *S. aureus*, the wounds on the PPV skin patch light group become dry and did not get a suppuration sign, which remained uninfected and got scabby on day 4 post-infection, implying an excellent anti-infection ability of the PPV skin patches *in vivo*. To gain visual insight into the *in vivo* therapeutic effects of the PPV skin patches, the spread plate assay of the tissue dispersions originating from the *S. aureus* infectious wound sites on day 1 and day 4 post-infection were performed accordingly. As shown in Fig. 4e, the infection group and the PPV skin patch dark group still displayed numerous *S. aureus* colonies, and the PPV skin patch light group exhibited nearly no bacterial colonies on day 1 and day 4 post-infection owing to the toxic ROS produced by PPV skin patches, further demonstrating the outstanding antibacterial performance of PPV skin patches *in vivo*. Next, the infected wound tissues on day 4 post-infection of the three groups were subjected to hematoxylin and eosin (H&E) staining for the histology analysis. As presented in Fig. 4f, numerous immune cells were found in the wound sections of infection and the PPV skin patch dark group, whose chromatin exhibited an aggregate state and were stained blue, implying a severe bacterial infection. However, the wound section of the PPV skin patch light group showed fewer immune cells and a clean H&E staining result. The results confirmed that the PPV skin patches printed from the Gel/Alg/HA/PPV ink could effectively kill bacteria *in vitro* and *in vivo*, and could also show the protection biofunction when a skin trauma occurred.

Besides protecting the body from bacterial invasions, the biofunction of artificial skin patches to facilitate tissue regeneration is another key issue to be considered. Improving the cell affinity of the Gel/Alg/HA/PPV ink could provide a feasible solution. As discussed in the introduction, A5G81 with the sequence of Ala-Gly-Gln-Trp-His-Arg-Val-Ser-Val-Arg-Trp-Gly-Cys (AGQWHRVSVRWGC, chemical structure is shown in Fig. S3a, ESI†) is a newly reported functional peptide aiming to enhance the cell affinity. Prior to covalently linking to HA, the cell safety, cell migration- and cell attachment-promoted effects of the A5G81 peptide were explored. As shown in Fig. S3b (ESI†), hMSCs exhibit high cell viability after incubation with a high concentration of the A5G81 peptide for 24 h, 48 h and 72 h, respectively, indicating its promising cell safety. Subsequently, cell migration and cell attachment experiments were designed as model assays to investigate the wound healing-promoted effects. The cell migration-promoted capability of A5G81 was evaluated by a cell scratch assay. Fig. S3c (ESI†) shows the cell migration images in the scratched areas after incubated with 0 μg mL^{-1} and 25 μg mL^{-1} A5G81 peptide. hMSCs exhibited a significantly higher migration ability after cultured with the A5G81 peptide than the control group. Fig. S3e (ESI†) summarizes the cell migration distances in the tested period. Compared to the cell migration distances (144 μm for 12 h, 301 μm for 18 h and 374 μm for 24 h) of the control group, A5G81 could vigorously promote cell migration (305 μm for 12 h, 458 μm for 18 h and 476 μm for 24 h). Moreover, as shown in Fig. S3d (ESI†), the images also indicated the robust cell attachment-promoted ability of the A5G81 peptide. When the cells were seeded in the plates without A5G81, only 58, 105 and 117 cells could attach on the plates in 2 h, 4 h and 18 h post-seeding. However, 167, 261 and 285 cells could successfully

realize cell attachment and elongation on 2 h, 4 h and 18 h post-seeding under the promotion of A5G81 (Fig. S3f, ESI†). It could be concluded that A5G81 had promising cell safety and significant capabilities to enhance cell migration and cell attachments.

The excellent biosafety, cell migration- and cell attachment-promoted effect of A5G81 peptide paved the way to incorporate A5G81 to HA thereby enhancing the cell affinity of the artificial skin patches. As displayed in Fig. S4a (ESI†), A5G81 was covalently linked to HA through the Michael addition reaction between maleimide groups on HA and thiol groups of cysteine at the C-terminus of the A5G81 peptide. Fig. S4b (ESI†) exhibits the ^{1}H-NMR spectra of A5G81, HA-A5G81 and HA in D_2O, respectively. HA-A5G81 displays classic peaks of A5G81 assigned at δ = 0.6–0.8 (α), 6.9–7.5 (ε) and 8.5 (ζ), and also shows classic peaks of HA assigned at δ = 1.7–1.9 (β) and 2.7–4.0 (γ), which demonstrated the successful covalent modification of A5G81 on HA. However, due to the high molecular weight of the selected HA (over 1 million), it was hard to calculate the modification ratio. Alternatively, the modification ratio of A5G81 on HA-A5G81 was detected to be 71.8 μg mg^{-1} through a standard TNBS assay (Fig. S4c and d, ESI†). By mixing HA-A5G81 with unmodified HA, the concentration of A5G81 could be tuned to 12.5 μg mg^{-1} and 25 μg mg^{-1} (fixing the mass ratio as 4% w/v Gel + 2% w/v Alg + 1% w/v HA). To investigate the enhanced-cell affinity of the Gel/Alg/HA-A5G81/PPV skin patches after A5G81 modification, cell attachment on the Ca^{2+}-crosslinked Gel/Alg/HA-A5G81/PPV ink was explored. As presented in Fig. S4e and f (ESI†), when the cells were seeded on the Gel/Alg/HA/PPV skin patches without A5G81, only 26 and 54 cells could attach on the skin patch after 2 h and 4 h post-seeding. When increasing the concentration of A5G81 to 12.5 μg mg^{-1}, 157 and 174 attached-cells were found after 2 h and 4 h post-seeding. Further increasing the concentration of A5G81 to 25 μg mg^{-1} induced an insignificant improvement of the attached cell numbers. In addition, live/dead confocal laser scanning microscopy (CLSM) images exhibited that a strong green signal was observed in the calcein-AM channel, while a negligible red signal was found in the propidium iodide (PI) channel, implying that hMSCs attached on the Gel/Alg/HA-A5G81/PPV skin patches were all alive, further demonstrating the low cytotoxicity and the excellent biocompatibility of the Gel/Alg/HA-A5G81/PPV skin patches (Fig. S4g, ESI†). According to the results presented in Fig. S3 and S4 (ESI†), the cell affinity of the Gel/Alg/HA-A5G81/PPV skin patches was indeed improved by augmenting cell migration and cell attachments, which was thereby anticipated to work for promoting the wound healing process.

To evaluate the promoted wound-healing ability of the fabricated highly bioactive Gel/Alg/HA-A5G81/PPV skin patches, the full-thickness excisional wound model on rats were utilized for the investigations. Fig. 5a illustrates the wound healing process. The Gel/Alg/HA-A5G81/PPV or Gel/Alg/HA/PPV skin patches were implanted to the wound sites, respectively, after the full-thickness skin trauma, while photography and data statistics of the wound area were conducted during the healing period. Fig. 5b shows the images of the wound sites in the

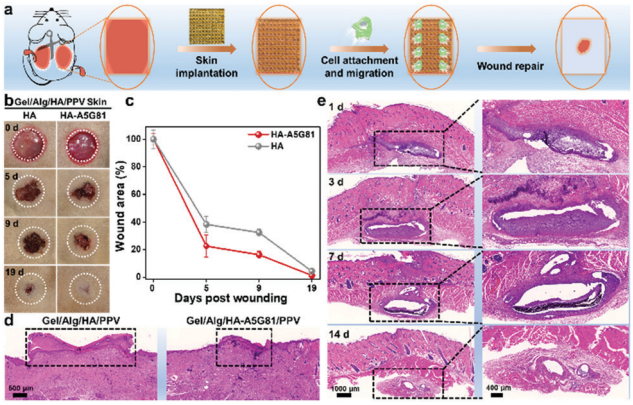

Fig. 5 Accelerated wound healing and *in vivo* biodegradability of the Gel/Alg/HA-A5G81/PPV skin patches. (a) Schematic of investigating the accelerated wound healing of Gel/Alg/HA-A5G81/PPV skin patches by a wound model on rats. (b) Representative images of the wounds treated with Gel/Alg/HA-A5G81/PPV or Gel/Alg/HA/PPV skin patches at 0 d, 5 d, 9 d and 19 d post wounding. (c) Wound area curve of Gel/Alg/HA-A5G81/PPV or Gel/Alg/HA/PPV skin patch group. (d) H&E Staining of the wound sites with treatment with Gel/Alg/HA/PPV and Gel/Alg/HA-A5G81/PPV skin patches at 19 d post wounding, respectively. The unhealed wound width was indicated with a dash square. (e) H&E Staining of Gel/Alg/HA-A5G81/PPV skin patch-implanted sites after 1 d, 3 d, 7 d and 14 d treatments, respectively.

healing process, and the wounds in the Gel/Alg/HA-A5G81/PPV skin patch group display better healing than that in the Gel/Alg/HA/PPV skin patch group. In the 19 days post wounding, the wounds in the Gel/Alg/HA-A5G81/PPV group almost healed, while they were non-healing in the control group without A5G81, implying the higher cell affinity and healing ratio of the Gel/Alg/HA-A5G81/PPV skin patches. The quantitative analysis of the wound healing process also indicated the higher healing rate of the Gel/Alg/HA-A5G81/PPV skin patches. As shown in Fig. 5c, on 5 days and 9 days post wounding, there was only 22.5% and 16.2% wound area left in the Gel/Alg/HA-A5G81/PPV skin patch group, while 38.3% and 32.4% left in the control group, further demonstrating their accelerated wound healing ability. Subsequently, the histological analysis was performed to evaluate the quality of the regenerated skin tissue after a 19 days treatment with the developed artificial skin patches. As displayed in Fig. 5d and Fig. S5 (ESI†), the wound of the Gel/Alg/HA-A5G81/PPV skin patch group almost healed, and the regeneration of the new tissues was also achieved, while the wounds in the Gel/Alg/HA/PPV skin patch group were still scabby and did not achieve the complete skin tissue regeneration. Moreover, the histological analysis was subsequently used to assess the biodegradability of the developed Gel/Alg/HA-A5G81/PPV skin patches, which was subcutaneously implanted on the rat model. The artificial skin patches could be clearly found in the subcutaneous wound sites, and they were gradually degraded over time. In the first 3 days post wounding, little artificial skin patches were biodegraded. However, they were significantly degraded in the 3–7 days post wounding, while nearly almost totally degraded in 14 days post wounding (Fig. 5e). Thus, the artificial skin patches printed from the Gel/Alg/HA-A5G81/PPV

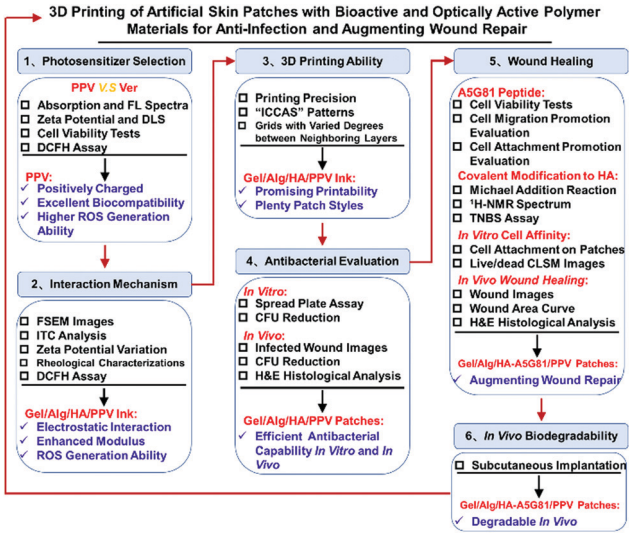

Scheme 2 Schematic of the overall workflow for 3D printing antibacterial skin patches with bioactive and optically active polymer materials for anti-infection and augmenting wound repair.

ink could promote the skin soft tissue regeneration owing to its high cell affinity, and could be biodegraded *in vivo*, exhibiting outstanding potentials in functional tissue regeneration.

Conclusions

In summary, a new conjugated polymer ink Gel/Alg/HA-A5G81/PPV was designed for human skin patch fabrication by the 3D printing strategy (Scheme 2). PPV imparted the skin patches with excellent PDT-based therapeutics against *S. aureus*, while HA-A5G81 exhibited promising cell affinity, which made the fabricated-artificial skin patch to exhibit the dual biofunctions of anti-infection and promoting soft tissue regeneration. Unlike the previously reported strategies, the 3D printing technology indeed diversified the microstructure and style of the artificial skin patches, thereby confirming its superiority. Compared to other hydrogel system-based dressings, the developed skin patches herein with integrated antibacterial ability, tissue regeneration-promoted capacity and plenty of microstructure styles were more suitable to work as skin equivalents, when skin trauma occurred. This work provides an advanced conjugated polymer ink for functional tissue/organ regeneration through 3D printing. By further exploring the biofunctions of conjugated polymers and following the ink design principle here, more functional inks can be proposed to assist the development of regenerative medicines.

Author contributions

H. Z.: conceptualization, data curation, formal analysis, investigation, methodology, writing–original draft. J. X.: data curation, methodology. H. Y.: methodology. E. Z.: methodology. N. D.: methodology. Z. G.: methodology. Y. H.: validation, formal analysis, writing–review & editing. F. L.: formal analysis, writing–review & editing. L. L.: visualization, writing–review & editing. Q. G.: funding acquisition, project administration, resources, supervision, validation, writing–review & editing. S. W.: conceptualization, funding acquisition, project administration, resources, supervision, validation, writing–review & editing.

Conflicts of interest

There are no conflicts to declare.

Acknowledgements

The work was supported by the Strategic Priority Research Program of the Chinese Academy of Sciences (XDA16020804 and XDA16020802) and the National Natural Science Foundation of China (No. 22021002, 22020102005).

Notes and references

1 K. A. U. Gonzales and E. Fuchs, *Dev. Cell*, 2017, **43**, 387.
2 B. K. Sun, Z. Siprashvili and P. A. Khavari, *Science*, 2014, **346**, 941.
3 D. Gan, T. Xu, W. Xing, X. Ge, L. Fang, K. Wang, F. Ren and X. Lu, *Adv. Funct. Mater.*, 2019, **29**, 1805964.
4 M. Kurita, T. Araoka, T. Hishida, D. D. O'Keefe, Y. Takahashi, A. Sakamoto, M. Sakurai, K. Suzuki, J. Wu, M. Yamamoto, R. Hernandez-Benitez, A. Ocampo, P. Reddy, M. N. Shokhirev, P. Magistretti, E. N. Delicado, H. Eto, K. Harii and J. C. I. Belmonte, *Nature*, 2018, **561**, 243.
5 H. Zhao, J. Xu, K. Peng, X. Fu, E. Zhang, F. Lv, L. Liu, N. Zhang, Y. Wang, S. Wang and Q. Gu, *Adv. Healthcare Mater.*, 2019, **9**, 1901295.
6 L. Shi, X. Liu, W. Wang, L. Jiang and S. Wang, *Adv. Mater.*, 2019, **31**, 1804187.
7 W. Li, K. Dong, J. Ren and X. Qu, *Angew. Chem., Int. Ed.*, 2016, **55**, 8049.
8 Y. Liang, X. Zhao, T. Hu, B. Chen, Z. Yin, P. X. Ma and B. Guo, *Small*, 2019, **15**, 1900046.
9 H. Yuan, Y. Zhan, A. E. Rowan, C. Xing and P. H. J. Kouwer, *Angew. Chem., Int. Ed.*, 2020, **59**, 2720.
10 S. V. Murphy and A. Atala, *Nat. Biotechnol.*, 2014, **32**, 773.
11 M. Hospodiuk, M. Dey, D. Sosnoski and I. T. Ozbolat, *Biotechnol. Adv.*, 2017, **35**, 217.
12 N. Noor, A. Shapira, R. Edri, I. Gal, L. Wertheim and T. Dvir, *Adv. Sci.*, 2019, **6**, 1900344.
13 B. Grigoryan, S. J. Paulsen, D. C. Corbett, D. W. Sazer, C. L. Fortin, A. J. Zaita, P. T. Greenfield, N. J. Calafat, J. P. Gounley, A. H. Ta, F. Johansson, A. Randles, J. E. Rosenkrantz, J. D. Louis-Rosenberg, P. A. Galie, K. R. Stevens and J. S. Miller, *Science*, 2019, **364**, 458.
14 M. M. Laronda, A. L. Rutz, S. Xiao, K. A. Whelan, F. E. Duncan, E. W. Roth, T. K. Woodruff and R. N. Shah, *Nat. Commun.*, 2017, **8**, 15261.
15 D. Joung, V. Truong, C. C. Neitzke, S.-Z. Guo, P. J. Walsh, J. R. Monat, F. Meng, S. H. Park, J. R. Dutton, A. M. Parr and M. C. McAlpine, *Adv. Funct. Mater.*, 2018, **28**, 1801850.

16 L. Koch, A. Deiwick, S. Schlie, S. Michael, M. Gruene, V. Coger, D. Zychlinski, A. Schambach, K. Reimers, P. M. Vogt and B. Chichkov, *Biotechnol. Bioeng.*, 2012, **109**, 1855.
17 L. J. Pourchet, A. Thepot, M. Albouy, E. J. Courtial, A. Boher, L. J. Blum and C. A. Marquette, *Adv. Healthcare Mater.*, 2017, **6**, 1601101.
18 B. S. Kim, G. Gao, J. Y. Kim and D.-W. Cho, *Adv. Healthcare Mater.*, 2019, **8**, 1801019.
19 L. Ma, C. Gao, Z. Mao, J. Zhou, J. Shen, X. Hu and C. Han, *Biomaterials*, 2003, **24**, 4833.
20 S. J. Hollister, *Nat. Mater.*, 2005, **4**, 518.
21 J. Liu, J. Chi, K. Wang, X. Liu, J. Liu and F. Gu, *Int. J. Clin. Exp. Pathol.*, 2016, **9**, 11197.
22 J. A. Rowley, G. Madlambayan and D. J. Mooney, *Biomaterials*, 1999, **20**, 45.
23 B. Yao, R. Wang, Y. Wang, Y. Zhang, T. Hu, W. Song, Z. Li, S. Huang and X. Fu, *Sci. Adv.*, 2020, **6**, eaaz1094.
24 L. Li, N. Wang, X. Jin, R. Deng, S. Nie, L. Sun, Q. Wu, Y. Wei and C. Gong, *Biomaterials*, 2014, **35**, 3903.
25 M. C. Giano, Z. Ibrahim, S. H. Medina, K. A. Sarhane, J. M. Christensen, Y. Yamada, G. Brandacher and J. P. Schneider, *Nat. Commun.*, 2014, **5**, 4095.
26 S. Li, S. Dong, W. Xu, S. Tu, L. Yan, C. Zhao, J. Ding and X. Chen, *Adv. Sci.*, 2018, **5**, 1700527.
27 B. Hu, Y. Shen, J. Adamcik, P. Fischer, M. Schneider, M. J. Loessner and R. Mezzenga, *ACS Nano*, 2018, **12**, 3385.
28 R. Qi, N. Zhang, P. Zhang, H. Zhao, J. Liu, J. Cui, J. Xiang, Y. Han, S. Wang and Y. Wang, *ACS Appl. Mater. Interfaces*, 2020, **12**, 17220.
29 (*a*) H. Chen, S. Li, M. Wu, Kenry, Z. Huang, C.-S. Lee and B. Liu, *Angew. Chem., Int. Ed.*, 2020, **59**, 632; (*b*) H. Zhu, J. Li, X. Qi, P. Chen and K. Pu, *Nano Lett.*, 2018, **18**, 586; (*c*) B. M. Luby, C. D. Walsh and G. Zheng, *Angew. Chem., Int. Ed.*, 2019, **58**, 2558; (*d*) H. Yuan, B. Wang, F. Lv, L. Liu and S. Wang, *Adv. Mater.*, 2014, **26**, 6978.
30 C. Zhu, L. Liu, Q. Yang, F. Lv and S. Wang, *Chem. Rev.*, 2012, **112**, 4687.
31 Y. Wang, L. Feng and S. Wang, *Adv. Funct. Mater.*, 2019, **29**, 1806818.
32 S. Liu, H. Yuan, H. Bai, P. Zhang, F. Lv, L. Liu, Z. Dai, J. Bao and S. Wang, *J. Am. Chem. Soc.*, 2018, **140**, 2284.
33 Y. Zhu, Z. Cankovaa, M. Iwanaszkob, S. Lichtorc, M. Mrksicha and G. A. Ameera, *Proc. Natl. Acad. Sci. U. S. A.*, 2018, **115**, 6816.